

# Size-Distribution and Emission Spectroscopy of W Nanoparticles Generated by Laser-Assisted CVD for Different WF<sub>6</sub>/H<sub>2</sub>/Ar Mixtures

Lars Landström,<sup>†,\*</sup> Jun Lu,<sup>‡</sup> and Peter Heszler<sup>§,#</sup>

The Ångström Laboratory, Department of Materials Chemistry, Uppsala University, Box 538, S-751 21 Uppsala, Sweden, The Ångström Laboratory, Department of Analytical Materials Physics, Uppsala University, Box 534, S-751 21 Uppsala, Sweden, and The Ångström Laboratory, Department of Solid State Physics, Uppsala University, Box 534, S-751 21 Uppsala, Sweden

Received: February 5, 2003; In Final Form: August 11, 2003

Tungsten nanoparticles were produced by ArF excimer laser-assisted chemical vapor deposition from WF<sub>6</sub>/H<sub>2</sub>/Ar gas mixtures. Subsequent pulses excited the gas-phase particles, allowing optical emission spectroscopy to monitor the intensity of the emitted radiation and temperature of the laser-heated particles. A systematic study on size-distributions of the deposited particles, determined by electron microscopy, in connection with emission spectroscopy and rate of deposition measurements is presented, with respect to different partial pressures of the reactants. The rates of deposition of W nanoparticle films were determined by X-ray fluorescence spectroscopy. In addition, the intensity of the scattered 193 nm laser line was also monitored as the partial pressure of H<sub>2</sub> was varied.

## Introduction

Nanoparticles and nanocrystalline materials often exhibit unique properties well differing from bulk, e.g., size-dependent melting point and optical characteristics, e.g., absorption and scattering cross-sections for single particles. Furthermore, collective properties such as increased hardness, super-plasticity, and improved magnetic properties are also observed in nanomaterials.<sup>1,2,3</sup>

Numerous methods exist for nanoparticle generation, e.g., mechanical (ball-milling),<sup>4</sup> template based,<sup>5</sup> sol-gel,<sup>6</sup> or gas-phase processes (e.g., gas condensation, chemical vapor deposition (CVD), etc.),<sup>7</sup> where the particles are condensed from an oversaturated vapor. The use of a laser to assist chemical vapor deposition (LCVD) during nanoparticle production introduces an extra well-controlled parameter in terms of energy and timing of the energy deposition if pulsed laser-sources are used.

LCVD of tungsten thin films from WF<sub>6</sub>/H<sub>2</sub> gas mixtures is an established metalization process, where the photolysis step either lowers the deposition temperature or increases the deposition rate.<sup>8</sup> However, at certain pressures and gas compositions, tungsten nanoparticles are formed,<sup>9</sup> and it is worth noting that no particles could be detected without H<sub>2</sub>, stressing the importance of CVD processes for nanoparticle formation. Particle formation during film deposition is an undesirable effect, but on the other hand it can be utilized for nanoparticle and/or nanomaterial fabrication. Because the particles are formed by homogeneous nucleation in the gas-phase, subsequent laser pulses heat up the particles that allows optical emission spec-

troscopy (OES) measurements on the laser induced light emission, which was identified as thermal (blackbody-like) radiation.<sup>10</sup>

The unique properties of nanomaterials have a significant (sometimes critical) size-dependence on the nm sized building elements. Thus, the understanding of the formation processes is of great importance in order to control the particle size and achieve narrow size-distributions. In our earlier papers on W nanoparticle formation during LCVD using WF<sub>6</sub> precursor, the optical spectroscopy studies were not coupled to size-distribution and rate of deposition measurements.<sup>9,10,11</sup> Therefore, in this report, results on size-distribution and deposition rate measurements are presented and related to optical spectroscopy of the light emission originating from the nanoparticles for different mixtures of the WF<sub>6</sub>/H<sub>2</sub>/Ar precursors, i.e., varying both the WF<sub>6</sub> and H<sub>2</sub> partial pressures. It is shown that by applying simple OES measurements the optimal precursor gas composition for achieving narrow particle size-distribution can easily be monitored.

In addition, inelastic quenching effects between the nanoparticles and ambient gas were also examined based on OES.

## Experimental Section

The experimental setup consisted of a stainless steel vacuum chamber with quartz windows at the front (laser beam in) and on top of the reactor, respectively. The flow-through reactor had a cross-section of ~12 cm<sup>2</sup>, and the laser induced light emission was observed perpendicularly to the laser beam through the top window of the chamber. The laser beam was slightly focused by a 38 cm focal length cylindrical lens. The place of optical observation was situated 9 cm downstream with respect to the WF<sub>6</sub>/H<sub>2</sub> inlet. An optical detection system consisting of a Czerny-Turner type grating spectrograph, a charge coupled device (CCD) detector, and an optical multi-channel analyzer (OMA III of EG&G) was used. A 150/mm grating allowed 1.8 nm spectral resolution and ±0.2 nm wavelength accuracy.

\* To whom correspondence should be addressed. E-mail: Lars.Landstrom@mkem.uu.se. Tel: +46 (0)18 471 3769. Fax: +46 (0)18 513 548.

<sup>†</sup> Department of Materials Chemistry.

<sup>‡</sup> Department of Analytical Materials Physics.

<sup>§</sup> Department of Solid State Physics.

<sup>#</sup> Also at Research Group on Laser Physics of the Hungarian Academy of Sciences, Zzeged, Box 406, H-6721 Hungary.

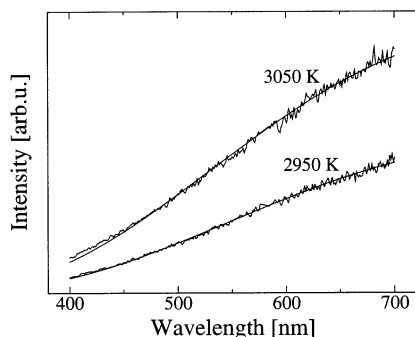


**Figure 1.** Typical corrected OES spectra from the laser-heated W nanoparticles. Delay 500 ns and gate pulse 1  $\mu$ s. Smooth solid line represents best fit by corresponding Planck curve.<sup>10</sup>

The gateable CCD detector was set to a 500 ns delay with respect to the laser pulse, and a 1  $\mu$ s gate pulse with overall exposure time of 1 s was used during OES measurements. Typical corrected OES spectra, with the best fit Planck curves and corresponding temperatures, are shown in Figure 1. The 500 ns delay was used to avoid uncertainties for the fitting procedure on the thermal radiation, because at shorter delays the high temperature of the nanoparticles resulted in evaporation of excited W atoms, and the de-excitation of these could be observed as superimposition of W elemental lines on the thermal radiation.<sup>12</sup>

The relative transfer function of the OMA was determined by using a tungsten-strip calibration lamp, that of the emissivity variation over the visible region was less than 0.5%. Measured spectra were corrected by the relative transfer function and, to determine the temperature of the nanoparticles, fitted by corresponding Planck curve, where the emissivity of tungsten nanoparticles was found proportional to  $\lambda^{-1.43}$  in the observed spectral region (400–700 nm),<sup>10</sup> where  $\lambda$  is the wavelength of the emitted radiation. Because a gate pulse of 1  $\mu$ s was used, an average temperature during this interval was observed. The integrated intensity was obtained by summation of the thermal emission in the monitored wavelength-window.

The measurements of intensity of the scattered 193 nm laser line were performed at 90°, relative to the excitation, with an acquisition time of 1 s.

A constant total pressure of 2000 Pa was used while varying the Ar, H<sub>2</sub>, and WF<sub>6</sub> partial pressures (Ar was introduced as purge-gas on the front window to prevent deposition on it). The H<sub>2</sub> partial pressure was varied between 0 and 1000 Pa with a constant WF<sub>6</sub> partial pressure of 30 Pa. WF<sub>6</sub> was varied between 0 and 170 Pa with constant H<sub>2</sub> partial pressure at 165 Pa. The linear gas velocity was held constant at 2 cm/s during all experiments; that is, the H<sub>2</sub> + Ar partial pressure was constant when H<sub>2</sub> was varied, and WF<sub>6</sub> + Ar was constant as WF<sub>6</sub> varied.

Laser parameters were as follows; wavelength 193 nm (Lambda Physik ArF excimer laser), nominal pulse duration 15 ns (fwhm), and repetition rate 50 Hz. The laser fluence at the place of optical observation and deposition was set to 120 mJ/cm<sup>2</sup> during all experiments.

Rates of deposition were measured for a constant deposition time (10 min) by X-ray fluorescence spectroscopy (XRF) by integrating the W<sub>L $\alpha$</sub>  peak for different partial pressures of the precursors WF<sub>6</sub> and H<sub>2</sub>. In addition, the intensity of the scattered laser line was also monitored as the H<sub>2</sub> partial pressure was varied.

For determination of the size distributions, particles were deposited on carbon covered Cu-grids for transmission electron microscopy (TEM) analysis.

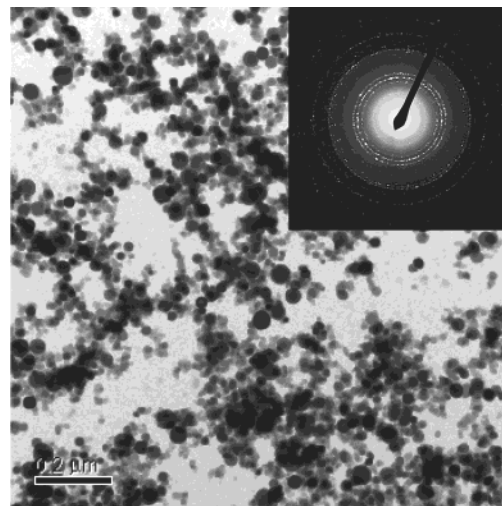


**Figure 2.** TEM BF picture of deposited particles at 120 mJ/cm<sup>2</sup> laser fluence, 165 Pa H<sub>2</sub> and 115 Pa WF<sub>6</sub> partial pressures, respectively, with electron diffraction pattern as inset.

## Results

Tungsten nanoparticles were formed by photolytic LCVD of different WF<sub>6</sub>/H<sub>2</sub>/Ar gas mixtures. A TEM bright field (BF) picture of the particles is shown in Figure 2. As can be seen, the particles have a regular round shape and are well distinguishable even though some agglomeration has occurred. The electron diffraction pattern originating from the particles (inset in Figure 2) corresponds well to  $\beta$ -W, a metastable phase that is assumed to be impurity stabilized.<sup>13,14</sup> Energy dispersive X-ray spectroscopy showed low concentrations of contaminants such as fluorine and oxygen, which supports the assumption of impurity stabilization. (X-ray photoelectron spectroscopy on deposited nanoparticle films also revealed O and F contamination, but the amount incorporated in the nanoparticles could not be determined with sufficient accuracy because of, e.g., post-oxidation of deposited particles and adsorbed tungsten subfluorides.<sup>15</sup>)

In parts a and b of Figure 3, the intensity of thermal emission and particle temperature dependence on the H<sub>2</sub> partial pressure ( $p_{\text{H}_2}$ ) are shown, respectively. In Figure 3a, it can be seen that the intensity of the emission increases rapidly until  $p_{\text{H}_2} \sim 50$  Pa. Then the intensity is almost constant for some tens of Pa after which the intensity decreases with increasing  $p_{\text{H}_2}$ . Normalized intensity, calculated using Stefan–Boltzmann's radiation law and temperatures from Figure 3b, is also shown in Figure 3a ( $\times$ ).

The temperature is approximately constant ( $\sim 3400$  K at 500 ns delay and 1  $\mu$ s gate pulse) above the threshold partial pressure (where a sufficient number of particles are formed to allow measurements with reasonable statistics) up to  $\sim 100$  Pa, see Figure 3b. Above this  $p_{\text{H}_2}$  the temperature decreases linearly ( $\sim -0.5$  K/Pa) with increasing  $p_{\text{H}_2}$ .

Size-distribution histograms for five different  $p_{\text{H}_2}$ 's are shown in Figure 4. It can be seen that the geometric mean diameter is  $\sim 12$  nm for all examined partial pressures, and only a slight increase in mean diameter of the particles is observed, see also Figure 5a. log–probability plots for the first two H<sub>2</sub> partial pressures (Figure 6, top panels) show a deviation from a log-normal size-distribution, and as the H<sub>2</sub> partial pressure is increased, this deviation remains (see Figure 4). The dependence of the rate of deposition of tungsten on  $p_{\text{H}_2}$  is shown in Figure 5b. A steep increase of the XRF signal can be observed up to  $\sim 60$  Pa, after which the rate of deposition is saturated and

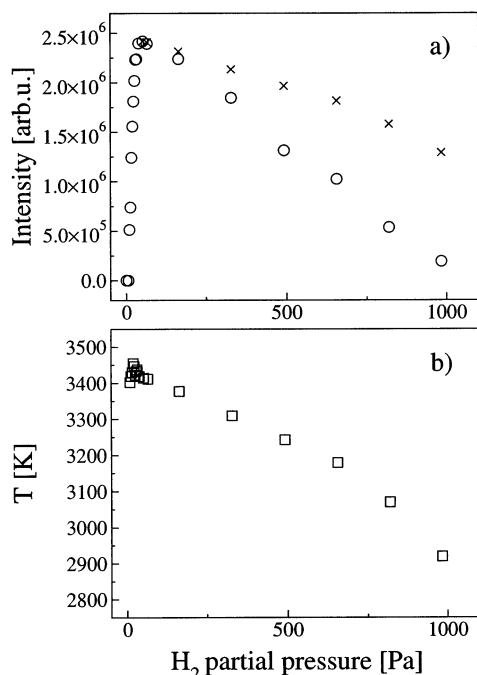


**Figure 3.** Integrated intensity of the thermal radiation (a) and temperature (b) of the particles (at 500 ns after the laser pulse and using 1  $\mu$ s gate pulse) vs H<sub>2</sub> partial pressure. WF<sub>6</sub> partial pressure 30 Pa with a total pressure of 2000 Pa. Data marked by  $\times$  in Figure 3a were calculated by using Stefan–Boltzmann’s radiation law and the measured temperatures in Figure 3b.

approximately constant up to 500 Pa (it is noted that for LCVD of thin films with comparable experimental parameters, the deposition rate of tungsten was found to be  $\sim 10$  nm/min<sup>16</sup>). Above this value a slight increase of the integrated intensity ( $W_{L_a}$ ) can be observed. The intensity of the scattered laser line, see Figure 5c, follows approximately the same behavior as the rate of deposition depicted in Figure 5b.

Intensity of thermal emission and dependence of the W nanoparticle temperature on WF<sub>6</sub> partial pressure ( $p_{WF_6}$ ) are depicted in Figure 7, parts a and b, respectively. A rapid increase of the intensity up to a partial pressure of  $\sim 30$  Pa can be observed, after which the intensity decreases slowly to a local minimum at  $\sim 75$  Pa (see Figure 7a). Then the intensity increases again to a maximum point at  $\sim 110$  Pa only to decrease again on further increase of  $p_{WF_6}$ .

As for the nanoparticle temperature dependence on  $p_{WF_6}$  (see Figure 7b), it can be seen that the temperature decreases approximately linearly ( $\sim -1.5$  K/Pa) until a partial pressure of  $\sim 120$  Pa WF<sub>6</sub>, after which the temperature drops rapidly ( $\sim -10$  K/Pa) with increasing  $p_{WF_6}$ .

Size-distributions of the generated W particles for different WF<sub>6</sub> partial pressures are shown in Figure 8. Only at the lowest  $p_{WF_6}$  (15 Pa), does the distribution follow the log-normal type (see also Figure 6). At higher  $p_{WF_6}$  ( $> 30$  Pa), this deviation (from a log-normal distribution) becomes more significant, and it can be seen that the mean size of the particles increases and that the distributions are broadened.

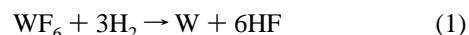
The rate of deposition of tungsten increases continuously as  $p_{WF_6}$  is elevated, slightly deviating from a linear behavior, see Figure 9a, and a threshold value for W nanoparticle generation seems to be present. The geometric mean volume of the particles follows an approximate linear dependence on  $p_{WF_6}$  (for  $p_{WF_6} \geq 15$  Pa), as can be seen in Figure 9b, but it should be noted that the extrapolated intercept (for  $p_{WF_6} = 0$ ) is situated on the

negative y axis. Again, this negative intercept suggests that a threshold value in  $p_{WF_6}$  has to be reached for nanoparticle formation.

## Discussion

**Relevant Processes.** To explain the experimental results, several chemical and physical processes have to be considered, and the most relevant are listed and discussed below.

The net chemical reaction for tungsten formation from WF<sub>6</sub> and H<sub>2</sub> precursors is



The dominant reaction pathway for particle formation during LCVD of W contains several steps, and most likely (i) the photolytic generation of sub-fluorides (mostly WF<sub>3</sub> and WF<sub>4</sub>), (ii) formation of W–W bonds between the sub-fluorides, and (iii) further reduction by H<sub>2</sub> are the most important.<sup>17</sup> After the particles are formed, they travel downstream by the gas-flow and are heated by following laser pulses (because the particles are still within the reaction zone). The temperature of these laser-heated particles, shortly after the laser pulse, will be independent of nanoparticle size in the first approximation, since the specific heat of one particle is proportional to  $r^3$  (volume) and the absorption cross-section of a particle also varies with  $r^3$  for spherical particles much smaller than the incident wavelength.<sup>18</sup> Considering that certain cooling mechanisms, e.g., evaporation, radiative and heat transfer by ambient, exhibit size-dependent rates of cooling which are not proportional to  $r^3$ , the rate of decrease of temperature is somewhat size-dependent. However, this effect is not taken into consideration in this work.

Thermal CVD (TCVD) processes on the surface of the nanoparticles may also be significant for the particle growth in a certain temperature range.<sup>10</sup> (The deposition rate expression for TCVD is proportional to  $p_{H_2}^{1/2}$  and  $p_{WF_6}^0$ .)<sup>19</sup> However, the particles reach high temperatures (see Figures 3b and 7b), and taking into account the delay time and temperature decreasing rate,<sup>12</sup> one can deduce that the initial temperature of the particles is very close to the melting point of tungsten ( $\sim 3695$  K) shortly after each laser pulse. This gives rise to high evaporation rates of tungsten atoms;<sup>12</sup> furthermore, the rates of desorption for the reactants in eq 1 at high temperatures are largely unknown. Therefore, an estimation of the net effect from these two competing processes becomes very uncertain.

Intensity of the emitted thermal radiation ( $I$ ) from the laser-heated particles follows Stefan–Boltzmann’s radiation law, i.e.

$$I = \int_0^\infty n_c(r) A_s(r) \epsilon(r) T^4 dr \quad (2)$$

where  $n_c$  is the size-distribution function of the particles in the observed volume,  $\epsilon$  is the emissivity,  $A_s$  is the surface area,  $r$  is the radius of the particle, and  $T$  denotes the absolute temperature.

The total LCVD produced tungsten mass is considered to be proportional to  $p_{WF_6}$  (within most of the investigated partial pressure region, see Figure 9a), so it follows that  $\int n_c r^3 \propto p_{WF_6}$  and, because  $\epsilon \propto r$  (ref 18) and  $A_s \propto r^2$ , eq 2 can be rewritten as

$$I \propto p_{WF_6} T^4 \quad (3)$$

However, eqs 2 and 3 are only valid until agglomeration of particles occurs. For agglomerated particles (e.g., fractal-like structures), interference effects of the light emission from the particles within the aggregates has to be taken into consideration.

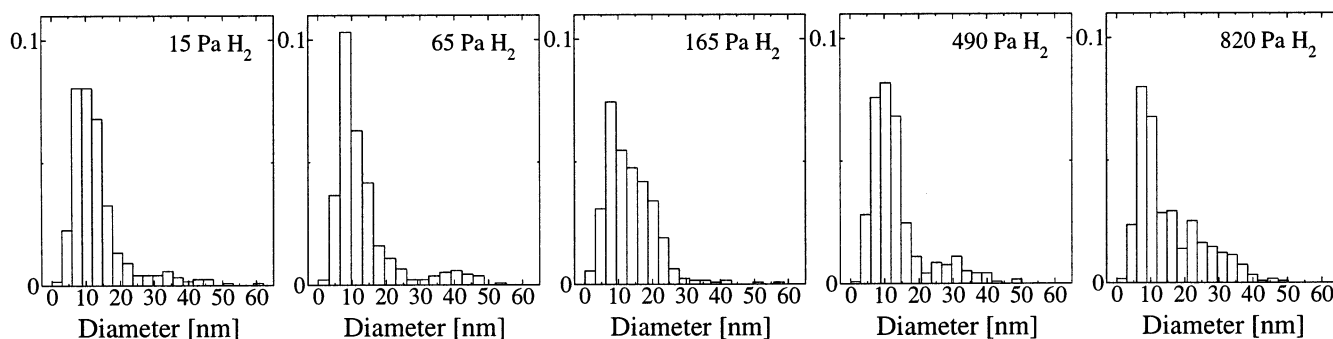


**Figure 4.** Normalized size-distribution histograms (sample size  $\sim 400$  from TEM BF micrographs) for five different  $H_2$  partial pressures.  $WF_6$  partial pressure 30 Pa with a total pressure of 2000 Pa.

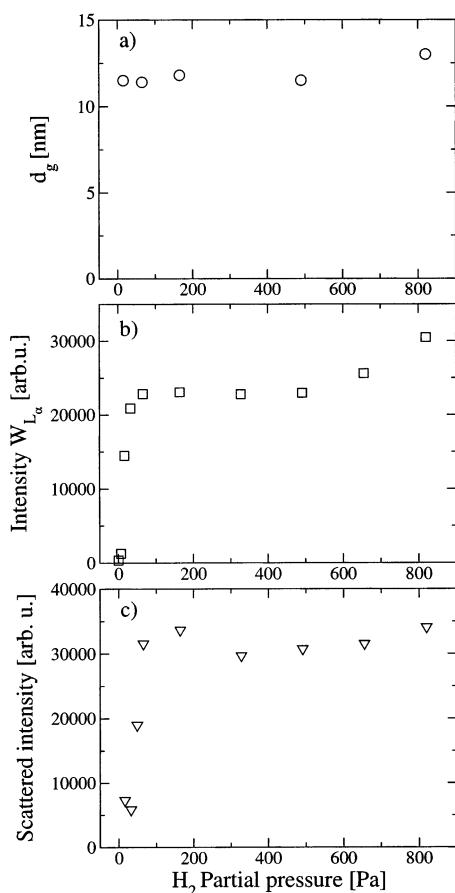


**Figure 5.** (a) Geometric mean diameter ( $d_g$ ), (b) tungsten deposition rate, in measures of the intensity of the  $W_{La}$  peak from XRF analysis, and (c) intensity of scattered 193 nm laser line dependence on  $H_2$  partial pressure, respectively. Total pressure 2000 Pa with a constant  $WF_6$  partial pressure of 30 Pa.

OES measurements were performed with a 1  $\mu s$  gate pulse, and during this time, the ambient gas collides with the particles, and some of these collisions quench the photon emission.<sup>9</sup> The amount of collisions ( $Q$ ) on a particle can be written as

$$Q = \frac{1}{4} \frac{p \langle v \rangle}{k_B T_a} A_s \quad (4)$$

where  $k_B$  is the Boltzmann constant,  $p$  is the pressure,  $\langle v \rangle$  is the mean velocity, and  $T_a$  is the temperature of the ambient gas (considered as room temperature, i.e., 295 K). Inelastic collisions

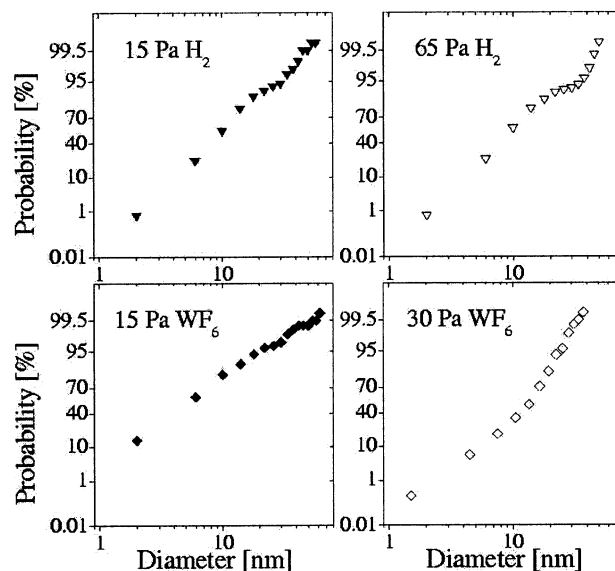


**Figure 6.** log-probability plots for the two first histograms in Figures 4 and 8, respectively. Only at 15 Pa  $WF_6$  partial pressure can a log-normal size-distribution be found.

also remove energy from the particles, and the energy dissipation per unit time ( $P$ ) can be described as<sup>20</sup>

$$P = \xi(l+1) \frac{1}{8} \frac{p \langle v \rangle}{T_a} A_s (T - T_a) \quad (5)$$

where  $l$  is the degrees of freedom for colliding molecule ( $l = 7$  and  $36$  for  $H_2$  and  $WF_6$ , respectively). The parameter  $\xi$  is the accommodation coefficient ( $\xi \leq 1$ ) and denotes the degree of inelasticity of the collisions.

As for the scattering from separated (noninterfering) gas-phase nanoparticles ( $r \ll \lambda$ ), the scattering cross-section follows the Rayleigh law; that is, the intensity is proportional to  $r^6/\lambda^4$ . Furthermore, the formation of gas-phase aggregates will also affect the intensity of the scattered light in a similar fashion as for the thermal radiation.

**$H_2$  Partial Pressure Dependence.** There is no significant change in the measured size-distributions as  $p_{H_2}$  is varied (see Figure 4). The observed distributions deviate from the log-normal type (see Figure 6, top panels), and this is explained by that agglomeration and further coalescence of the particles occur at  $\sim 30$  Pa  $p_{WF_6}$ . This assumption is verified in the following subsection.

Because of the chemistry of the net reaction (see eq 1), no particles can be formed if no  $H_2$  is present, which can be seen in Figure 3a (no thermal radiation was observed at zero  $H_2$

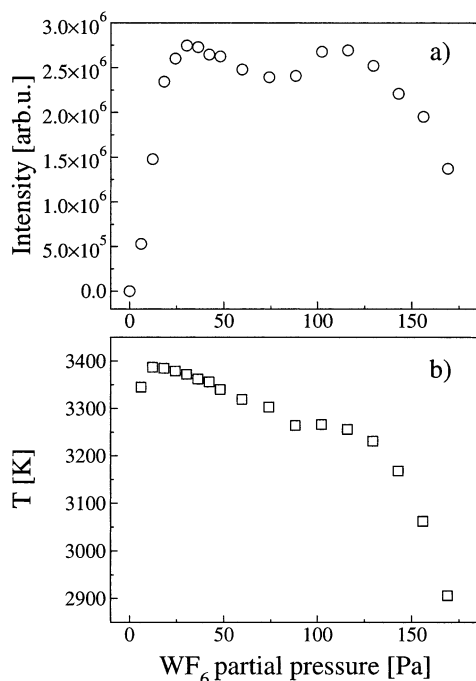


**Figure 7.** Intensity of the thermal radiation (a) and temperature of the generated W particles (b) vs WF<sub>6</sub> partial pressure. Gate pulse 1  $\mu$ s, delay time 500 ns, H<sub>2</sub> partial pressure 165 Pa with a total pressure of 2000 Pa.

partial pressure). When a certain threshold value is reached ( $\sim 10$  Pa), the number of generated particles allow sufficient statistics for the optical measurements. Above this threshold value, the intensity increases rapidly with  $p_{\text{H}_2}$ , which indicates that the particle concentration ( $n_c$ ) also increases rapidly according to eq 2, considering that the temperature and mean size of the particles are approximately constant (see Figures 3b and 5a). This is interpreted as that in the  $\sim 10$ – $50$  Pa  $p_{\text{H}_2}$  interval access of H<sub>2</sub> within the reaction-zone is in deficit with respect to the 30 Pa WF<sub>6</sub> partial pressure, in analogy with eq 1. The maximum intensity is observed at  $\sim 60$  Pa H<sub>2</sub>, and this suggests that a saturation of the total volume of generated tungsten nanoparticles is reached (for the experimental parameters and setup used). This is confirmed by the rate of deposition and scattering measurements (see Figure 5). It is noted that, according to the stoichiometry of the net reaction (see eq 1), the maximum emitted intensity, in accordance with the partial pressure of WF<sub>6</sub> (30 Pa), should be found at 90 Pa H<sub>2</sub> partial pressure. This discrepancy is explained by the change in stoichiometry of the net reaction due to the photolytic contribution during LCVD.<sup>17</sup> (Less H<sub>2</sub> is needed for the tungsten formation since the laser photons strip away fluorine atoms.) Because neither significant decrease nor increase of the scattered intensity could be observed (at  $p_{\text{H}_2} > 60$  Pa) during the scattering experiments (see Figure 5c), a change in size of gas-phase aggregates is ruled out (at 30 Pa WF<sub>6</sub> an increasing number of aggregates was observed, see section C, and a change in size of these aggregates would otherwise alter the scattering characteristics).

The decrease of intensity of the thermal radiation after the observed maximum can be attributed to (i) a decrease of the temperature of the particles at elevated H<sub>2</sub> pressures (see Figure 3a), due to the increased heat conductivity of the gas mixture, and (ii) to quenching of the emission by collisions with excess H<sub>2</sub> molecules. The quenching is evident if one considers the intensity difference between calculated intensity (marked by  $\times$

in Figure 3a), based on measured temperatures in Figure 3b and the observed intensity ( $\circ$  in Figure 3a). The measured Stern–Volmer plot also gives evidence for the quenching of light emission.<sup>9</sup> The microscopic explanation of the increased heat conductivity of the gas mixture can be related to the increased number of inelastic collisions between H<sub>2</sub> molecules and W particles, resulting in a cooling of the particles as observed in Figure 3b. The measured data allow for the estimation of the degree of inelasticity ( $\xi$ ) of the H<sub>2</sub> collisions by using eq 5. The collision rate of H<sub>2</sub> molecules with a 12 nm in diameter particle (see Figure 5a) increases with H<sub>2</sub> partial pressure as  $\sim 50$  collisions/(Pa  $\mu$ s) according to eq 4. Thus, taking the gate pulse length (1  $\mu$ s) and the slope of Figure 3b into consideration,  $\xi$  was calculated and found to be  $\sim 0.15$ . (This value should be interpreted as that 15% of the maximum allowed energy,  $E_{\text{max}}$ , is transferred as an average for every H<sub>2</sub> molecule – W nanoparticle collision.  $E_{\text{max}} = C_{\text{H}_2}(T - T_a)$  where  $C_{\text{H}_2}$  is the heat capacity of a H<sub>2</sub> molecule.)

The nearly constant mean size of the particles and deposition rate (Figure 5, parts a and b) as  $p_{\text{H}_2}$  was varied is in line with earlier results on photolytic LCVD of tungsten from WF<sub>6</sub> precursor, where the rate of deposition was found being independent of  $p_{\text{H}_2}$  above a threshold value.<sup>22</sup> The slight mean size increase at high  $p_{\text{H}_2}$  is most likely due to TCVD on the surface of the hot particles.<sup>10</sup>

**WF<sub>6</sub> Partial Pressure Dependence.** The WF<sub>6</sub> partial pressure dependence of intensity of thermal radiation and of the temperature are depicted in parts a and b of Figure 7, respectively. (Also recall that the total LCVD produced tungsten volume is increasing over the whole examined pressure range [see Figure 9a].)

If a similar size-distribution is assumed during the first, rapidly increasing part, the intensity increase (at low  $p_{\text{WF}_6}$ ) can be attributed to an increasing number of particles (see eq 2, considering a constant temperature [see Figure 7b]). At a certain critical concentration, collisions between the particles will be significant resulting in agglomeration in the gas phase. As a consequence, the coalescence in the agglomerates results in a distortion of the initial size distribution. This distortion can easily be seen in Figures 6 and 8, where a deviation from log-normal distribution begins at  $\sim 30$  Pa. Agglomerated particles can also be seen in Figure 2 ( $p_{\text{WF}_6} = 115$  Pa), which confirms the aggregation of the nanoparticles.

In the 30–120 Pa partial pressure region, the behavior of the emitted light intensity is connected to the formation of gas-phase aggregates. Further and detailed investigations of these phenomena, concerning emission from aggregates, are in progress in connection with light scattering measurements from aggregated W nanoparticles.<sup>21</sup>

At  $\sim 120$  Pa WF<sub>6</sub>, the intensity of the emission starts to decrease, and this change can be explained by attenuation of the laser beam due to increased absorption of the generated particles and the precursor gas at elevated  $p_{\text{WF}_6}$  (e.g.,  $\sim 35\%$  of the incident laser light is absorbed by WF<sub>6</sub> molecules at  $p_{\text{WF}_6} = 120$  Pa).

The linear decrease of temperature (see Figure 7b) up to  $\sim 120$  Pa is explained by inelastic collisions between the nanoparticles and WF<sub>6</sub> molecules, in combination with an attenuation of the laser beam. The collision rate of WF<sub>6</sub> molecules with a 12 nm in diameter particle increases with WF<sub>6</sub> partial pressure as  $\sim 4$  collisions/(Pa  $\mu$ s), but the high number of degrees of freedom for WF<sub>6</sub> results in an effective quenching, see eq 5. Above  $\sim 120$  Pa the temperature drops rapidly (see Figure 7b), which confirms the laser attenuation.

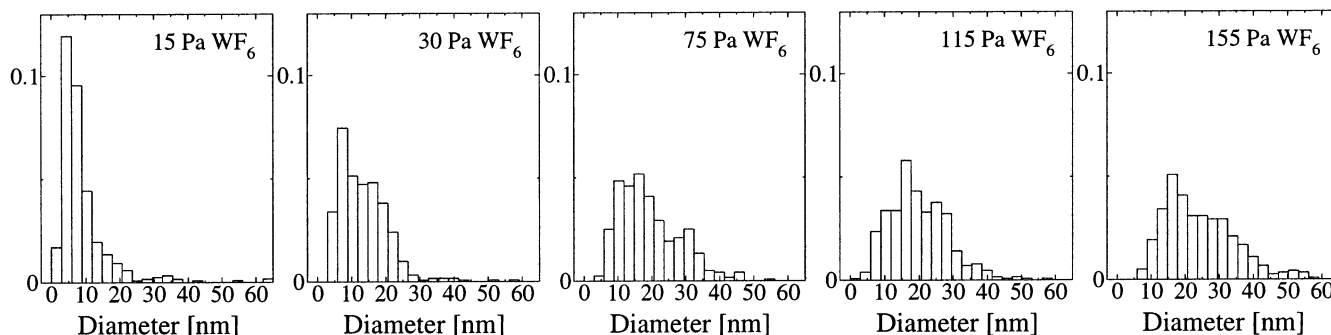


**Figure 8.** Normalized size-distribution histograms (sample size  $\sim 400$  from TEM BF micrographs) for five different  $\text{WF}_6$  partial pressures.  $\text{H}_2$  partial pressure 165 Pa with a total pressure of 2000 Pa.

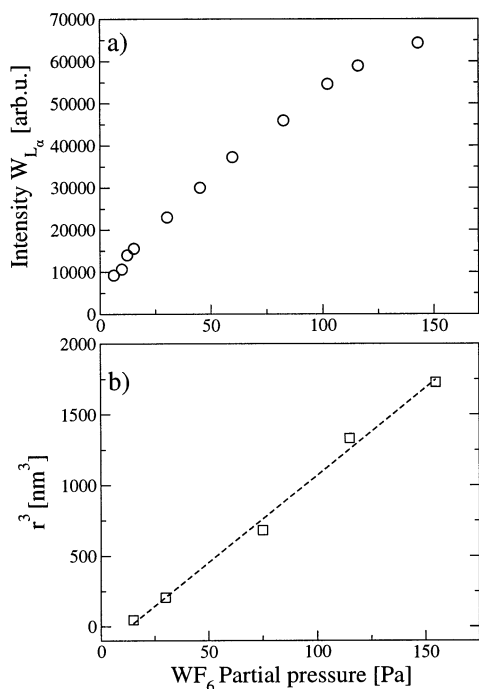


**Figure 9.** (a) Rate of deposition of tungsten from XRF measurements and (b) cubic geometric mean radius, from Figure 8, dependence on  $\text{WF}_6$  partial pressure.  $\text{H}_2$  partial pressure 165 Pa at a total pressure of 2000 Pa. The dashed line in part b represents the best linear fit.

The rate of deposition of W increases close to linearly up to  $\sim 80$ – $90$  Pa  $\text{WF}_6$  (see Figure 9) which is consistent with earlier studies.<sup>22</sup> Extrapolation of the measured XRF signal to  $p_{\text{WF}_6} = 0$  indicates that a threshold value of generated sub-fluorides has to be reached for nanoparticle formation. At  $p_{\text{WF}_6} > 80$ – $90$  Pa, a slower increase of deposition rate, compared to lower partial pressures, is observed and is explained by two effects: (i) the  $\text{H}_2$ : $\text{WF}_6$  ratio is less than 2, resulting in less tungsten formation according to the net reaction (eq 1 and taking into account the photolytic contribution) and (ii) the attenuation of the incoming laser light due to absorption and scattering from precursor molecules and generated W particles.

Recall that the intercept (in particle mean volume dependence, see Figure 9b) is situated on the negative y axis. This confirms the above statement that a threshold value for  $p_{\text{WF}_6}$  exists for generation of tungsten nanoparticles.

**On the Observed Size Distributions.** If the particles are formed during an equilibrium condensation from an oversaturated vapor, with constant oversaturation ratio, the expected result is a log-normal distribution of the particles.<sup>23</sup> Below the so-called coagulation limit (the point where significant coalescence takes place), the residence time approach (RTA) model

can be applied to explain the resulting log-normal distribution.<sup>24</sup> In the RTA model, the particle growth is assumed to be governed purely by vapor condensation and that no aggregation or coagulation of particles occur. Furthermore, a log-normal distribution can also be preserved above the coagulation limit, if the total mass is conserved and a sufficient number of collisions takes place, because of the self-preserving behavior of the coagulation process and initial distribution.<sup>25</sup>

Log-normal size distributions were found at low  $\text{WF}_6$  partial pressures ( $< 30$  Pa) in accordance with the RTA model (see Figure 6). At high oversaturation ratios (i.e., above the coagulation limit at high  $\text{WF}_6$  partial pressures), distorted distributions were found instead of preserved initial (log-normal) distributions. Because an open system was used, the total mass of the generated particles was not conserved, and in addition, the residence time in the reaction-zone was small ( $\sim 4.5$  s). These facts explain the distorted distributions (relative to log-normal and shifted toward larger diameters) for high partial pressures of  $\text{WF}_6$  ( $> 30$  Pa).

To obtain narrow size distribution, one has to avoid the agglomeration/coagulation, and for that, a low  $\text{WF}_6$  partial pressure is needed. (If higher  $p_{\text{WF}_6}$  is used, the critical point in particle concentration for aggregation/coagulation can also be shifted by decreasing the residence time.) The  $\text{H}_2$  partial pressure is almost irrelevant, with the exception that it has to exceed about twice of the value of  $p_{\text{WF}_6}$ . In addition, OES is capable of monitoring the agglomeration of the particles during LCVD, and precise evaluation of this phenomenon is under way.<sup>21</sup>

Modeling of the particle growth within the aggregates is in progress to understand the linear particle volume on  $\text{WF}_6$  partial pressure dependence when agglomeration of particles occurs.

## Conclusions

Size-distribution, temperature and intensity of emitted thermal radiation dependence of precursor composition was examined for LCVD generated tungsten nanoparticles from  $\text{WF}_6/\text{H}_2/\text{Ar}$  gas mixtures. The precursor gas composition was systematically varied and spectra of the emitted thermal (blackbody-like) radiation, originating from the laser-heated nanoparticles, was monitored by means of OES. Scattering measurements were also performed while varying the partial pressure of  $\text{H}_2$ .

Variation of the  $\text{H}_2$  concentration between 1 and 50% (at 1.5%  $\text{WF}_6$  concentration) did not result in significant change of the size-distributions, and only a slight increase in mean diameter was observed. A fast increase of the intensity of the thermal radiation was observed up to 3%  $\text{H}_2$ , indicating that an increasing number of particles were formed. However, above 3%  $\text{H}_2$  concentration, a decrease of both the emitted intensity and temperature of the particles could be observed because of (i) the quenching of excited states and (ii) an increased heat transfer

by the increasing number of H<sub>2</sub> collisions, respectively. The accommodation factor  $\xi$  (degree of inelasticity of the H<sub>2</sub>–W nanoparticle collisions) was found to be  $\sim 0.15$ . The rate of deposition of tungsten and the intensity of the scattered laser line dependence on H<sub>2</sub> partial pressure revealed that a saturation in W deposition was reached at  $\sim 3\%$  H<sub>2</sub>. This saturation was found at a WF<sub>6</sub>:H<sub>2</sub> ratio of 1:2 (instead of 1:3 ratio according to stoichiometry) and was explained by the photolytic contribution of the UV laser energy to the W deposition rate.

The rate of deposition of W dependence of WF<sub>6</sub> concentration increased almost linearly in the observed partial pressure range (0–8.5%), and the mean volume of the generated tungsten nanoparticles depended linearly on the WF<sub>6</sub> concentration. A rapid increase of the emitted thermal radiation could be observed up to 1.5% WF<sub>6</sub> (at 8% H<sub>2</sub> partial pressure). In the partial pressure range of 1.5–6%, the behavior of the intensity of emitted light can be explained by the formation of gas-phase aggregates. Importantly, size-distribution data verified this concept, because a broadening and shift of the distributions (due to agglomeration and further coalescence) was found above 1.5% WF<sub>6</sub> concentrations. Above 6% WF<sub>6</sub>, both the emitted thermal intensity and temperature of the W particles decreased rapidly because of increased absorption of the incident laser light by the WF<sub>6</sub> precursor molecules and the generated nanoparticles.

Log-normal and narrow size distributions were found for gas mixtures consisting of low WF<sub>6</sub> concentrations, where no significant agglomeration of the particles leading to coalescence occurred. Thus, to obtain narrow distributions, a low concentration of WF<sub>6</sub> should be used (independently of the H<sub>2</sub> concentration if  $p_{\text{H}_2} > 2p_{\text{WF}_6}$ ). Alternatively, the residence time within the reaction zone should be decreased if higher concentrations of WF<sub>6</sub> are to be used.

**Acknowledgment.** Financial support from the Swedish Research Council and Göran Gustafsson foundation is gratefully

acknowledged. One of the authors (P.H.) is also thankful for partial supports from the OTKA foundation with Grant Nos. T34381 and TS040759.

## References and Notes

- (1) Hayashi, C.; Uyeda, R.; Tasaki, A. *Ultra-Fine Particles*; Noyes Publications: New Jersey, 1997.
- (2) Nalwa, H. S. *Handbook of Nanostructured Materials and Nanotechnology*; Academic Press: San Diego, 2000.
- (3) Gleiter, H. *Acta Mater.* **2000**, *48*, 1.
- (4) Eckert, J.; Holzer, J. C.; Krill, C. E., III.; Johnson, W. L. *J. Mater. Res.* **1992**, *7*, 1751.
- (5) Huczko, A. *Appl. Phys. A* **2000**, *70*, 365.
- (6) Brinker, C. J.; Scherer, G. W. *Sol–Gel Science*; Academic Press: Boston, 1990.
- (7) Hahn, H. *Nanostruct. Mater.* **1997**, *9*, 3.
- (8) Shintani, A.; Tsuzuku, S.; Nishitani, E.; Nakatani, M. *J. Appl. Phys.* **1987**, *61*, 2365.
- (9) Heszler, P.; Mogyorósi, P.; Carlsson, J.-O. *J. Appl. Phys.* **1995**, *78*, 5277.
- (10) Heszler, P.; Landström, L.; Lindstam, M.; Carlsson, J.-O. *J. Appl. Phys.* **2001**, *89*, 3967.
- (11) Heszler, P.; Carlsson, J.-O. *Vacuum* **1995**, *46*, 955.
- (12) Landström, L.; Heszler, P. submitted.
- (13) Hägg, G.; Schönberg, N. *Acta Crystallogr.* **1954**, *7*, 351.
- (14) Tang, C. C.; Hess, D. W. *Appl. Phys. Lett.* **1984**, *45*, 633.
- (15) Landström, L.; Kokavecz, J.; Lu, J.; Heszler, P. submitted.
- (16) Mogyorósi, P.; Carlsson, J.-O. *J. Vac. Sci. Technol. A* **1992**, *10*, 3131.
- (17) Heszler, P.; Carlsson, J.-O.; Mogyorósi, P. *J. Vac. Sci. Technol. A* **1993**, *11*, 2924.
- (18) Bohren, C. F.; Huffman, D. R. *Absorption and scattering of light by small particles*; John Wiley & Sons: New York, 1983.
- (19) Hitchman, M. L.; Dobson, A. J. *Appl. Surf. Sci.* **1989**, *38*, 312.
- (20) Bäuerle, D. *Laser Processing and Chemistry*, 3rd ed.; Springer Verlag: Berlin, 2000.
- (21) Landström, L.; Heszler, P. to be published.
- (22) Matsuhashi, H.; Nishikawa, S.; Ohno, S. *Mater. Res. Soc. Symp. Proc.* **1989**, *129*, 63.
- (23) Scheibel, H. G.; Porstendorfer, J. *J. Aerosol Sci.* **1983**, *14*, 113.
- (24) Söderlund, J.; Kiss, L. B.; Niklasson, G. A.; Granqvist, C. G. *Phys. Rev. Lett.* **1998**, *80*, 2386.
- (25) Lai, F. S.; Friedlander, S. K.; Pich, J.; Hidy, G. M. *J. Colloid Interface Sci.* **1972**, *39*, 395.